A proper orthogonal decomposition analysis upon aerodynamic structures under clean and rough conditions

Ingrid Quiroga,[1] Ander Zarketa-Astigarraga,[2] Juan A. Cárdenas-Rondón,[1, a)] Alejandro Martínez-Cava,[1, a)] Markel Penalba,[2, b)] Alain Martin-Mayor,[2] and Manex Martinez-Agirre[2]

[1)] *ETSIAE-UPM, Universidad Politécnica de Madrid, Plaza Cardenal Cisneros 3, E-28040, Madrid, Spain*

[2)] *Mondragon Unibertsitatea, Faculty of Engineering, Mechanical and Industrial Production, Loramendi 4, Mondragon 20500 Gipuzkoa, Spain*

(*Electronic mail: azarketa@mondragon.edu.)

(Dated: 17 July 2023)

The transitional flow regime is known to induce complex flow structures upon aerodynamic geometries such as airfoils, and the dynamics of laminar separation bubbles (LSBs) pose a relevant research field. In addition to being affected by the Reynolds value itself, LSBs are shown to be equally sensitive to the surface roughness of the airfoils. The study analyses wind-tunnel-derived surface-pressure distribution data-sets obtained for a particular airfoil of the standard family developed by the National Advisory Committee for Aeronautics (NACA), namely the NACA0021, subjected to the range $0.8 \times 10^4 < \mathrm{Re} < 1.6 \times 10^4$ at different angles of attack under two flow configurations that correspond to a clean and a roughened surface. The analysis is undertaken via the proper orthogonal decomposition (POD) technique. The results show that the decomposition of the temporal series of surface-pressure data and the processing of the most energetic POD modes recovers the position of the LSBs, properly capturing the closure point of the separation bubbles and, hence, the turbulence transition location. Some of the most energetic POD modes observed are closely related, in terms of shape, to the POD modes present at the reattachment point on a 5:1 rectangular cylinder. This could indicate there is a recognizable pattern in the coherent structures of pressure fluctuations when it comes to a reattached flow. Therefore, a principal component analysis such as the POD presented in this study can be used to determine the reattachment position of the flow or the transition point in presence of a LSB.

I. INTRODUCTION

Micro- and nano-scale unmanned aerial vehicles (MAVs and NAVs, respectively), middle-scale wind-turbines and small aircrafts share the common feature of employing airfoil-based aerodynamics as their working principle. When compared to their large-sized counterparts, such as aircrafts or MW-rated wind-turbines, the particularity of the aforementioned devices is that their aerodynamic blades operate at much lower chord-based Reynolds numbers, usually falling within the $10^4 - 5 \times 10^5$ interval[1–10]. Those Reynolds values correspond to a flow regime known as transitional, within which the air develops in a complex manner, with the fluid structures that are common to both the laminar ($\mathrm{Re} \lesssim 10^4$) and turbulent ($\mathrm{Re} \approx 10^6 - 10^7$) regimes strongly interplaying[4,11]. The so-called laminar separation bubble (LSB) addresses a fluid structure characterized by a separation of the laminar flow from the airfoil surface and a further reattachment in the turbulent form, and is a feature of the transitional regime[11–14]. As developing LSBs are highly dependent on the freestream conditions of the flow such as the Reynolds number[15] or the surface-roughness of the airfoil[16–18], they may compromise the aerodynamic behavior of the airfoil with the subsequent difficulties for controlling the overall system.

A standard airfoil developed by the National Advisory Committee for Aeronautics (NACA), namely the NACA0021, has been subjected to a set of transitional Reynolds numbers under different flow paradigms, a its aerodynamic behaviour analysed experimentally in a set of previous works by the authors[19,20]. The dependence on the Reynolds number, or the so-called scale-effect, has been addressed to be relevant at Reynolds variations as low as 0.2×10^5, with the bubble structure being severely affected by the flow configuration, and the lift (c_l), drag (c_d) and surface-pressure (c_p) coefficients showing significant variations within the typical range of angles-of-attack[19]. Likewise, the aerodynamic behavior of the airfoil has been shown to depend strongly on the free-stream turbulence level and the surface-roughness condition of the device, with turbulence and roughness synergistically interplaying to yield aerodynamic efficiency ($E = c_l/c_d$) losses beyond 60% in the worst-case scenario, thus highlighting the relevance of considering both perturbing factors when testing turbine blades in wind tunnels[20] or through numerical analyses[21]. Furthermore, the transitional regime is characterised by the presence of aerodynamic hysteresis, a phenomena defined by a loop-like behavior of the lift coefficient due to the different stalling and recovery angles, and which has been studied by the authors in a previous study[20]. On the analysis of detached flows, Saathoff and Melbourne [22] enunciated that the areas of greatest variance of surface pressure fluctuations are related to the flow reattachment location. On this regard, Cardenas-Rondón *et al.* [23] completed a study on flow separation on rectangular cylinders employing the so-called Proper Orthogonal Decomposition (POD) technique. The analysis showed that the POD modes, whose energies are related to

[a)] Also at Instituto Universitario "Ignacio Da Riva" (IDR/UPM), Universidad Politécnica de Madrid

[b)] Also at Ikerbasque, Basque Foundation for Science, Euskadi Plaza 5, 48011 Bilbao, Spain

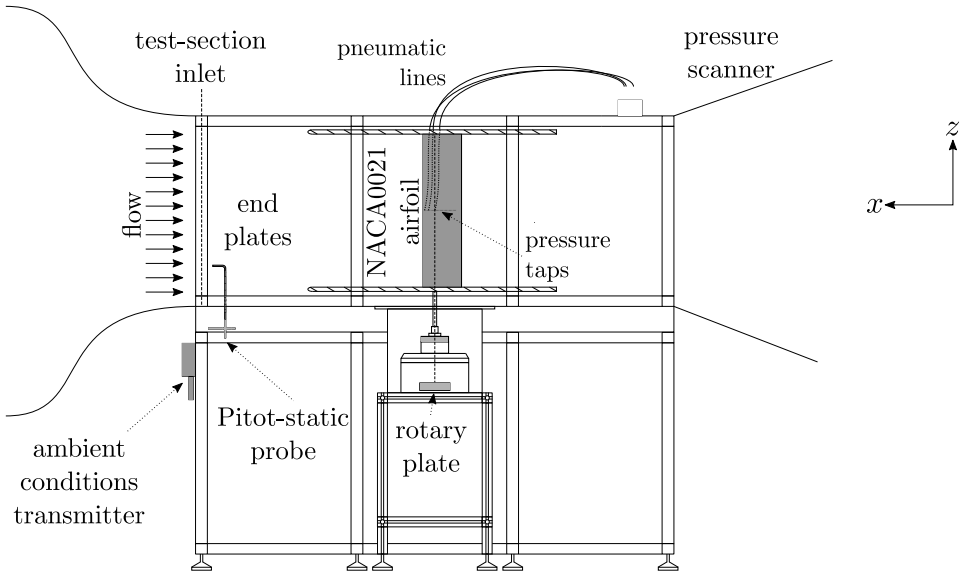

FIG. 1: Schematic illustration of the wind tunnel set-up for undertaking surface-pressure measurements upon an airfoil.

the variance of the signal (namely, the c_p time series), also present maximum amplitudes in areas where the flow reattaches, and can therefore be used to determine the LSB reattachment location. This numerical tool has been extensively used on the detection and identification of coherent structures developed in the flow[24,25], and on the generation of reduced-order models (ROMs) to reproduce non-linear aerodynamic phenomena[26,27].

Despite the aforementioned analysis on a NACA0021 airfoil operating transitionally, the mentioned studies merely provide a static description of the aerodynamic behavior. The experimental measurements undertaken for the analysis have been statistically averaged, and the provided results only show the mean values of the data-sets, concealing the information that corresponds to the inherent unsteady nature of the LSBs[11,28]. Analysing the unsteadiness of the LSBs is relevant insofar it may provide insights on two aspects: first, to achieve a better understanding on the characterization of transitionally-operating airfoils. Second, because it may pave the way towards potential flow-control techniques. There are several updated studies dealing with the unsteady and temporal behaviour of transitionally-operating airfoils and LSBs, employing modal analyses such as POD[29–31], or dynamic mode decomposition (DMD)[32]. Apart from providing insights on the laminar-to-turbulent transition, the addressed papers also show the relevance of considering surface-roughness effects on the airfoil behaviour, which may either be caused by environmental agents[33] or specifically implemented for enhancing the aerodynamics of the device[8,29,32]. Given the interest that such a research line is having lately, the present work recovers the raw data-sets obtained by Zarketa-Astigarraga *et al.* [19,20] on smooth (clean) and rough airfoil surfaces emulating degradation effects, which may take place, in real-world applications, due to environmental agents such as dust, ice or insect debris accumulation and erosion. Hence, the main goal of the present study is to perform a time-dependent analysis of the measured aerodynamic structures. For such a purpose, a POD technique is applied on the c_p distributions measured upon the surface of a NACA0021 airfoil. The POD eigenvectors associated with the separation and reattachment phenomena are here analyzed for a set of Reynolds numbers falling within the transitional regime. In particular, attention is put on characterizing the position of the LSB closure via the shape of the energetic modes provided by the POD. With the energy of the eigenmodes being directly related to the variance of the pressure signal the underlying boundary layer flow-physics on transitional airfoils retain a similarity with the aforementioned, as long as the reattachment position is known to fluctuate noticeably on the suction side. Underpinning its dynamic nature is relevant for fully describing the temporal evolution of the LSBs, thus gaining insights into a thorough characterization of the transitional regime in airfoils under realistic operational conditions. Finally, the construction of ROMs based on POD modes reveals the main differences between clean and rough airfoil configurations. The leading edge roughness appears to play a role on the downstream mixing and homogenization of the pressure fluctuations, hence needing a greater number of eigenmodes to recover the underlying flow physics through the ROM. The paper is structured so that Section II presents the experimental set-up, the measurement protocols and the surveying campaign. Section III provides a theoretical background on the POD technique, which is deemed necessary for following the subsequent discussion with effortlessly. Section IV is devoted to presenting the results derived from the research, as well as undertaking the corresponding discussions. Finally, Section V synthesises the main findings of the work and suggests possible future research lines.

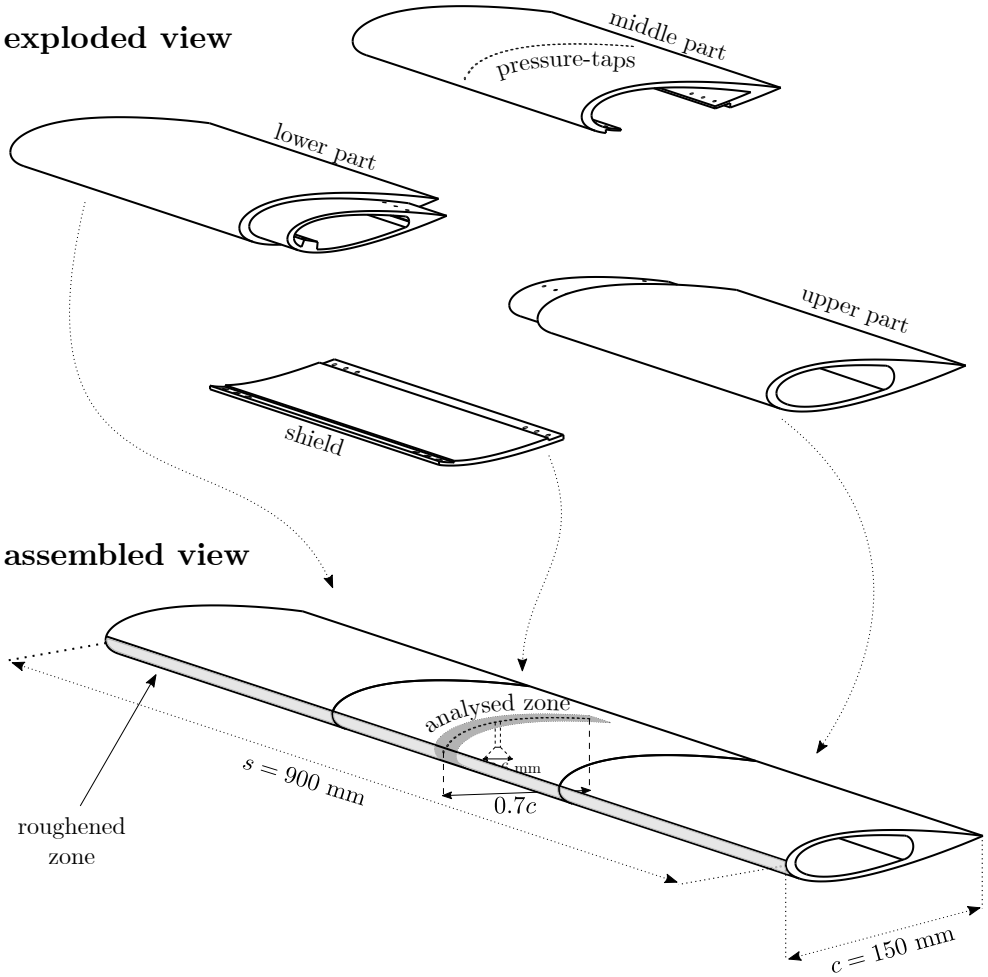

FIG. 2: Schematic illustration of the three-part assembly of the NACA0021 model with the probing region and the roughened zone highlighted.

II. EXPERIMENTAL SET-UP

The experiments are performed in an open-circuit suction-type wind tunnel driven by a 37 kW fan. The test-section of the tunnel has a rectangularly-shaped cross-section of 0.75×1 m^2, and is 3 meters long. The device has been designed for achieving flows with peak velocities of 40 m/s and turbulence levels below 0.2%. A more thorough information about the tunnel and its flow-related quality parameters are available in[34,35]. For illustrative purposes, FIG 1 provides a schematic draft of the set-up.

The tested airfoil consists of a symmetrical NACA0021 model, and has a chord-wise dimension of $c = 150$ mm and a span of $s = 900$ mm. Due to its relatively large spanwise dimension, the model has been manufactured in a three-piece modular form in order to ensure its structural integrity when being shaped via electrical discharge machining. A depiction of the model is given in FIG 2, with further details being available in[36]. The reason for choosing the NACA0021 model has to do with its application-agnostic nature, which allows focusing on the development of LSBs without considering the subtleties that may arise from a particular transitional application.

Pressure-taps are installed in a set of orifices that the airfoil has at its centre-line, and its hollow upper part allows taking the pneumatic lines to a pressure-measuring device placed atop the wind tunnel ceiling. A set of 30 orificies practiced upon the chord-wise extent of the airfoil's midspan serve as taps for undertaking surface-pressure measurements; the first and last orifices are placed at the leading-edge and at a $\approx$70% of the chord-wise stage respectively, leaving an average distance of a 3.6 mm between adjacent holes. The model is bounded by two endplates, leaving the necessary distance between the airfoil tips and the plates for ensuring the two-dimensionality of the flow[37]. The determination of the flow conditions at the airfoil rely on the value of the chord-based Reynolds number, computed by measuring the inlet velocity with a *Delta-Ohm HD49047T01L* Pitot-static probe and the ambient conditions via a *Delta-Ohm HD2001.1* transmitter. The pressure-measuring device corresponds to a *Scanivalve MPS4264* differential pressure scanner with a sampling-rate of 850 Hz.

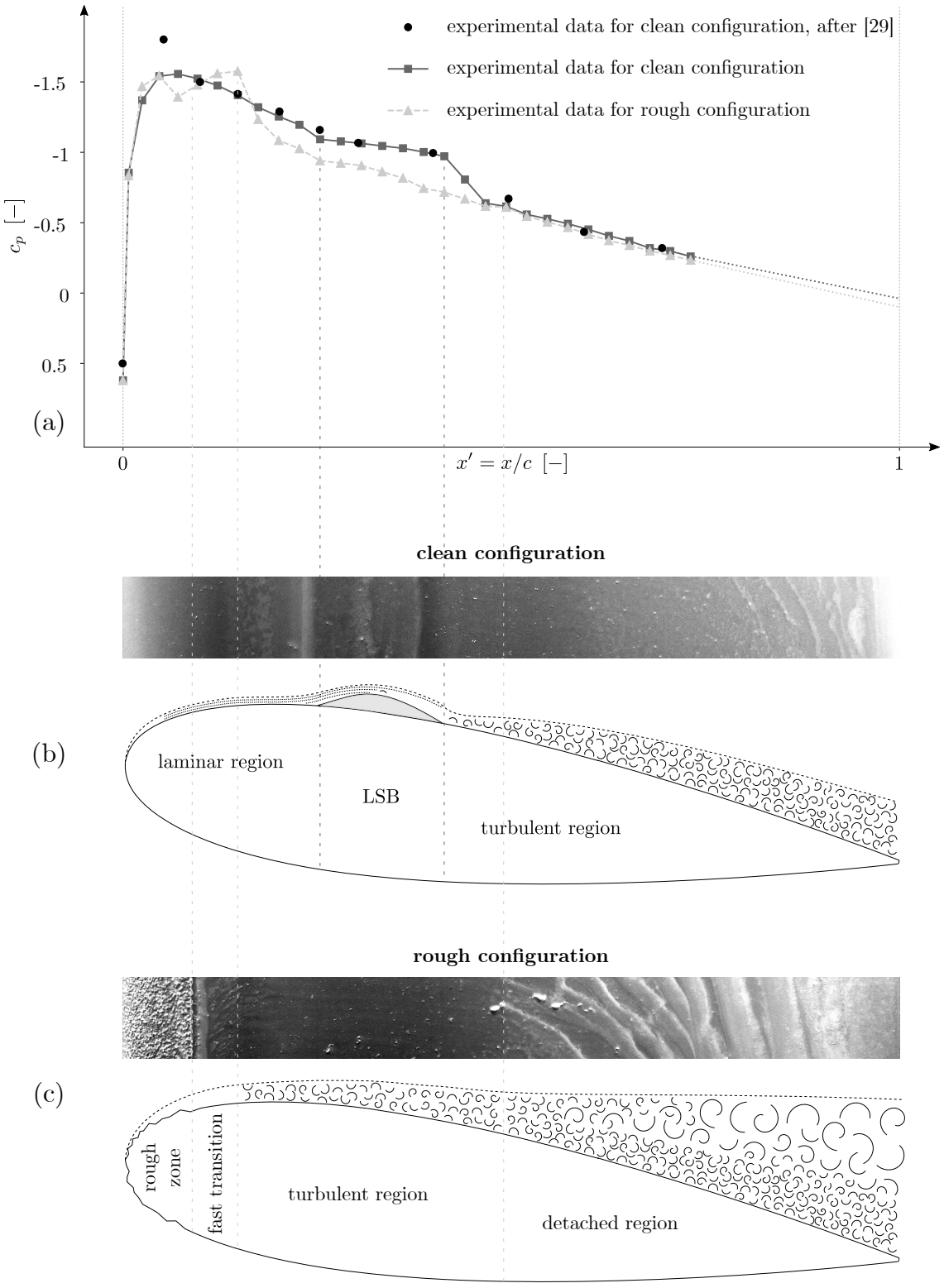

FIG. 3: (a) Suction-side $c_p - x'$ distributions for clean and rough configurations at Re$= 1.2 \times 10^5$ and $\alpha = 5°$, and validation data from[29]; (b) oil-flow visualisations for the clean configuration, and schematic of the fluid structures developed upon the suction-side; (c) oil-flow visualisations for the rough configuration, and schematic of the fluid structures developed upon the suction-side.

TABLE I: parametrical schedule for the experimental testing campaign.

Flow paradigm	**Reynolds number**	**Angular config.**	**Turbulent intensity (I)**	**# cases**
Clean	$\mathrm{Re} \in [0.8, 1, 1.2] \cdot 10^5$	$\alpha \in [0, 20]^\circ$, $\Delta\alpha = 1^\circ$	Default (0.2%)	3
		$\cup$		
Turbulent		$\alpha \in [20, 0]^\circ$, $\Delta\alpha = -1^\circ$	3.8%	3
				Total
				6

The measurement protocol proceeds by setting the tunnel at a given Reynolds number and angle-of-attack, and letting the flow stabilize for 2 seconds. Afterwards, a 5-seconds-long measurement is performed, which yields a $c_p - x'$ curve for such an angular configuration, with $x' = x/c$ being the dimensionless chord-wise variable. According to Barlow et al.[38], a statistically converged measurement requires a recording period as large as for letting a fluid particle travel a distance equivalent to 10 test-section lengths if the statistical independence of the recorded signal is to be ensured. For a 3-meters-long test-section, achieving such a statistical convergence with a 5-seconds-long measurement period corresponds to an inlet velocity as low as 6 m/s, which is the minimum value that the wind tunnel system is able to provide without choking the fan. Such a 5-seconds period is maintained for every measurement prescribed in the protocols below. The measurement process is repeated for each of the α values comprising the angular route. Such a route is defined so that it covers a cyclic path, comprising an increasing path spanning the range $\alpha \in [0, 20]^\circ$ with $\Delta\alpha = 1^\circ$, and a decreasing one that imposes angular decrements of $\Delta\alpha = -1^\circ$. The cyclic route allows capturing the aerodynamic hysteresis loop that ensues when stalling occurs[19]. The post-processing stage corrects the pressure measurements for a set of perturbing effects, such as the size and depth of the pressure-taps, the presence of burrs on their edges or the length of the pneumatic lines, according to Tropea et al.[39].

The flow reproduced with the configuration shown in FIG 1 corresponds to a steady, two-dimensional and uniform airstream and, accordingly, it is dubbed the clean-flow paradigm. Reproducing other flow configurations requires incorporating flow-perturbing effects within the tunnel. The additional flow paradigm considered in the current work corresponds to the rough flow. A roughened airfoil is achieved by implementing a sand-grained paper strip symmetrically at the leading-edge and covering the 10% extent of the chord-wise dimension as shown in FIG 2, thus emulating the region most prone to show degraded surface characteristics[17,40].

Thus, the flow paradigms reproduced herein correspond to two physical scenarios: a clean flow corresponding to default wind tunnel scenarios, and a rough flow that reproduces an airfoil with an environmentally damaged leading-edge surface. Experimental tests are undertaken at five different Reynolds numbers, namely $\mathrm{Re} = [0.8, 1.6] \times 10^5$ with $\Delta\mathrm{Re} = 0.2 \times 10^5$, thus covering a major extent of the transitional regime. The measurements performed at each of the case-studies yield $\alpha-$dependent chord-wise c_p distributions.

TABLE II: maximum, mean and standard deviations of the uncertainty intervals.

Flow paradigm	$\delta_{c_{p_{max.}}}$	$\overline{\delta_{c_p}}$	$\sigma_{\delta_{c_p}}$
Clean	0.4438	9.07×10^{-2}	1.45×10^{-2}
Turbulent	0.7899	0.2372	1.92×10^{-2}

In dimensionless terms, such distributions turn into $c_p - x'$ curves, $x' = x/c$ being the normalized chord-wise parameter. The multi-parametric set of variables for the overall experimental campaign is synthesized in TABLE I.

Experimental repeatability is ensured by carrying out a threefold set of measurements per case-study. An uncertainty analysis based on[35,41] is performed upon the data-sets, with the computed uncertainty intervals corresponding to a 95% confidence level. The maximum, mean and standard deviation values of the c_p uncertainty intervals are given in TABLE II.

FIG 3 serves for showing the data-sets obtained from the measurements, as well as providing both quantitative and qualitative evidence for the validity of the experiments. FIG 3a represents two suction-side c_p distributions against the normalised chordal distance (x'), obtained for the NACA0021 airfoil operating under a Reynolds number of 1.2×10^5 and an angle-of-attack of 5°; additionally, the experimental data coming from the study of Zhao et al. is plotted, measured for the same NACA geometry facing the slow under identical conditions[29]. As observed, the clean configuration of the present study matches the data-set of Zhao et al. acceptably. The differences lie below the corresponding experimental uncertainty interval shown in TABLE II except for the points lying either close to the suction peak or the reattachment region. However, such discrepancies may be assumable considering the sensitivity of the peak zone and the reattachment phenomenon. Likewise, the close morphological resemblance of both distributions make manifest that the fluid structures measured in the two studies agree.

FIG 3b shows an oil-flow visualisation of the configuration employed for validating the data, as well as the corresponding schematic of the fluid structures developed along the suction-side. The visualisation has been performed by painting the suction-side surface with a mixture of sunflower oil and titanium oxide (TiO_2) pigment and letting the flow sweep the oily layer for a period of 30 minutes, which is the average time required for making the fluid structure patterns steady

and visible, and thus representative enough of the average distributions of the suction-side. As shown, the laminar region corresponds to an effective sweeping of the mixture, and the LSB structure gets manifested as a zone of unperturbed oil, matching the plateau formed in the distribution of FIG 3a. The turbulent region after the reattachment phenomenon is correlated with a regain of the effective sweeping, although the trailing-edge region begins to show certain oil traces that mark the beginning of the detachment phenomenon. A more thorough explanation of the visualisation technique, as well as detailed interpretations of the flow patterns upon a set of clean configurations, is given in a previous paper by the authors[20].
FIG 3c is the counterpart of FIG 3b for the rough configuration. The roughness strip covering the 10% of the chordal distance is apparent, and the fast transition that occurs afterwards may be interpreted as the local accumulation of the oil layer in the immediate zone beyond the strip. The development of the turbulent region is again correlated with the effective sweeping of the layer, although the detachment phenomenon seems to ensue earlier than in the clean configuration. Even if the abscence of the LSB may be observed in the lack of a plateau-like region of the roughened distribution in FIG 3a, there is no much difference in the trailing-edge data-sets, even if the visualisations show completely different patterns therein. That is why such patterns are mainly employed as qualitative indicators of the flow structures being developed along the airfoil, and serve the sole purpose of showing that the quantitative measurements may be correlated with directly observable patterns.
Anyhow, the comparisons in FIG 3 sanction the validity of the c_p measurements upon which the following analysis depends, both quantitatively and qualitatively.

III. NUMERICAL ANALYSIS

The standard POD is a mathematical tool that allows dividing complex data into statistical coherent structures, also called "modes". This technique has been widely used not only in the aerodynamics field[42,43], but also in signal compression, process identification and control, structural analysis, oceanography, among several applications[44]. Analysing fluid flows configurations, there are different aims on the use of POD. On one hand, POD may be used to develop reduced-order models of complex flows, based on experimental analyses[23,45–47] or computational studies[48], by holding the most energetic modes describing the physics of the problem with a smaller amount of data. On the other hand, POD can be applied to analyse coherent flow structures, studding the spatial distribution of the modes and the associated time series[46,47].

The POD basic principles, when applied to a data gathered in aerodynamic wind tunnel testing with N_t pressure taps, are presented below. In order to get a complete overview of this tool, the interest reader is advised to consult the work of Schmidt and Colonius[49].

From the collected experimental data, an array constituted by the time series of the measured pressure values, $P(t_j)$, can be built as:

$$\mathbf{P}(t_j) = [\tilde{p}_1(t_j),\ \tilde{p}_2(t_j),\ \ldots\ ,\ \tilde{p}_{Nt}(t_j)]^{\mathrm{T}}, \tag{1}$$

where $\tilde{p}_i(t_j)$ is the pressure measured in tap i ($i = 1,\ 2,\ \ldots,\ N_t$) at the time instant t_j ($j = 1,\ 2,\ \ldots,\ N_s$, being N_s the number of samples). Each pressure time series can be decomposed according to:

$$\tilde{p}_i(t_j) = \bar{p}_i + p_i(t_j), \tag{2}$$

being $\bar{p}_i$ and $p_i(t_j)$ the mean value and the pressure fluctuations, respectively.

Following this decomposition, the mean value of each time series is subtracted from each time series, and the fluctuation pressure matrix, $\mathbf{p}(t_j)$, is obtained:

$$\mathbf{p}(t_j) = [p_1(t_j),\ p_2(t_j),\ \ldots\ ,\ p_{Nt}(t_j)]^{\mathrm{T}}. \tag{3}$$

Finally, the $N_t \times N_t$ covariance matrix of the fluctuations, $\mathbf{Cov}, \mathbf{p}$, is determined as:

$$\mathbf{Cov}\,(p_i, p_k) = \frac{1}{N_s}\sum_{j=1}^{N_s} p_i(t_j)p_k(t_j), \tag{4}$$

which eigendecomposition is performed through the associated eigenvalue problem:

$$(\mathbf{Cov}, \mathbf{p} - \lambda_\mathbf{i}\mathbf{I})\,\phi_\mathbf{i} = 0. \tag{5}$$

The eigenvectors, ϕ_i, and eigenvalues, λ_i, of the covariance matrix, estimated with (Equation (5)), correspond to the POD modes and their associated energy, respectively. The eigenvectors represent coherent spatial distributions of the pressure fluctuations extracted from the time series[49].

Once these modes are normalized, they can be organized into a modal matrix:

$$\Phi = [\phi_1,\ \phi_2,\ \ldots\ ,\ \phi_{N_t}], \tag{6}$$

being possible to obtain the time series associated with each mode, $a_i(t_j)$ as:

$$\mathbf{a}(t_j) = \Phi^{-1}\mathbf{p}(t_j). \tag{7}$$

These time series can be interpreted as the pressure fluctuations expressed in the POD eigenvectors modal space.

It can be shown that the correlation matrix of the time series associated with the POD modes, $\mathbf{Cov}, \mathbf{a} = \lambda_\mathbf{i}\mathbf{I}$, is diagonal, implying that the POD modes represent coherent structures that are not statistically correlated with each other. On the other hand, it can also be verified that the energy of each mode corresponds to the variance of its associated time series. On account of this, the most energetic modes correspond to the spatial structures of the pressure fluctuations that contribute the most variance to the complete solution.

As follows from expression (Equation (7)) pressure fluctuations time series, $\mathbf{p}(t_j)$, can be reconstructed from the POD modes, ϕ, and the time series associated to each mode, $\mathbf{a}(t_j)$, according to

$$\mathbf{p}(t_j) = \phi_1\mathbf{a}_1(t_j) + \phi_2\mathbf{a}_2(t_j) + \ldots + \phi_{Nt}\mathbf{a}_{Nt}(t_j), \tag{8}$$

note that the modes are column vectors and the time series are row vectors.

Therefore, it is possible to reconstruct the pressure fluctuations by summing only the contributions from the interest POD modes. In this way, reduced-order models (ROM) are generated to reconstruct the original signal by collecting only the most relevant eigenmodes information. The number of eigenvectors considered to generate a ROM is known as the model order. In Section IV E ROMs of different orders are used to analyse the influence of each mode on the physics of the flow.

IV. RESULTS AND DISCUSSION

In order to ease the description of the results, the discussion has been divided into a number of subsections that deal with separate blocks of the analysis. Section IV A introduces the main characteristics of the modal description, providing the minimal set of notions for following the rest of the discussion easily. Sections IV B and IV C proceed with the discussion by considering the sensitivity of the POD modes and energy-carrying structures with respect to the angle-of-attack and the Reynolds number, respectively. Section IV D establishes a comparison of the previously discussed modal characteristics between the clean- and rough-flow paradigms, showing the main effects induced when passing from a nominal blade to a degraded one. Lastly, Section IV E is devoted to the discussion of reduced-order models in the context of the POD technique applied to a transitionally-operating airfoil.

A. Layout of the results

The layout of the figures to be read is represented in FIG 4. The charts are divided into two groups. The left hand-side of the layout is reserved for plotting the eigenvalues of the modes calculated for the configurations to be represented. In the case of FIG 4a, a single case is plotted, which corresponds to the airfoil operating at $\alpha = 12^\circ$, Re = 1.2×10^5. It is to notice that the plot owns two $y-$axes; the left hand-side one shows the relative value of the eigenvalues, i.e. $\varepsilon = \lambda_i / \sum_{i=1}^{N_t} \lambda_i$, with such values represented by their respective bars. The right hand-side is the corresponding cumulative plot, namely $\tilde{\varepsilon} = \sum_{j=1}^{i} \lambda_j / \sum_{i=1}^{N_t} \lambda_i$. The $x-$axis stands for the modes themselves, i.e. ϕ_i.

Although the $y-$axes may seem to provide the same information, it is considered that the employed two-fold representation eases the analysis; the plot of the relative eigenvalues serves the purpose of showing the global distribution of the modes which, as observed, adopts the form of an exponential decay. This is a trend that has been observed in the overall set of data, meaning that the most representative modes are usually confined to the first 5 eigenvalues, indicating that the measured phenomena can be grouped into a few orthogonal contributions. Consequently, the analysis that follows will be restricted, at most, to those four modes. Besides, the cumulative plot is employed for representing the modal tendencies on a global manner, and allows distinguishing the contribution of the overall set of modes in a holistic way. Mind that, if the eigenvalues are represented in a relative basis, the cumulative plot ends at the normalized value of unity.

If the left hand-side of the figure allows depicting the global trends coming from the POD analysis, the right hand-side is devoted to showing the local features of the configuration. The two plots on the layout correspond, respectively, to the average c_p distribution (FIG 4b) and to the chord-wise spatial distribution of the eigenmodes (FIG 4c). Notice that the each of the subplots owns its own $y-$axis, but that they share the abscissa representing the dimensionless chord-wise parameter, i.e. $x' = x/c$. Additionally, mind that the $y-$axis of the c_p plot is inverted due to the fact that the represented curves correspond to the suction-side distributions, whose pressure values, accordingly, lie below the referential static pressure of the wind tunnel. Thus, the $x' - c_p$ curves are intended to show the local features of the flow, whereas the modal distributions provide the energetic account within such a local scope.

Thus, the purpose of the chosen layout is to provide a straightforward way of comparing the global and local features simultaneously. On the one hand, the idea is to relate the global energetic features with the local particularities of the flow and the modal distributions, which stands for the two left-to-right vectors in the figure. On the other hand, it is attempted to interpret the local flow and modal particularities together. The overall figure may be complemented by additional sub-figures in case it is deemed necessary to provide a clearer information, but that will not alter the general layout essentially.

B. Sensitivity to the angle-of-attack, α

A holistic view upon which to develop the analysis is shown in FIG 5. There are two sets of figures akin to the ones described in Section IV A. The first set is constituted by FIGS 5a and 5c to 5e, and corresponds to airfoil configurations at a Reynolds number of 1.2×10^5 and low angles-of-attack (i.e. $\alpha \in [1,5]^\circ$). The second set refers to FIGS 5b and 5f to 5h, and it attempts at giving a picture upon the overall range of tested angles-of-attack (namely $\alpha \in [0,20]^\circ$) for the same Reynolds number.

Proceeding with the first set of figures, it is to notice the predominance of the first mode in FIG 5a, although such a feature seems to decay progressively with the angle-of-attack. Anyhow, the relative flatness of the cumulative curves show that higher modes do not influence noticeably on the flow features. However, this is to be contrasted with the modal shapes shown in FIGS 5d and 5e. The former plot corresponds to the most energetic mode, whereas the latter refers to the second one. As observed, the first mode seems insensible to the angle-of-attack of the airfoil at low angles-of-attack, even if it constitutes the main energy-carrying structure. Furthermore, the progressive morphological evolution of the c_p curves shown in FIG 5c are not reflected on the first modal shapes. Such c_p distributions highlight the sensitivity that underlies the aerodynamics of transitionally-operating airfoils,

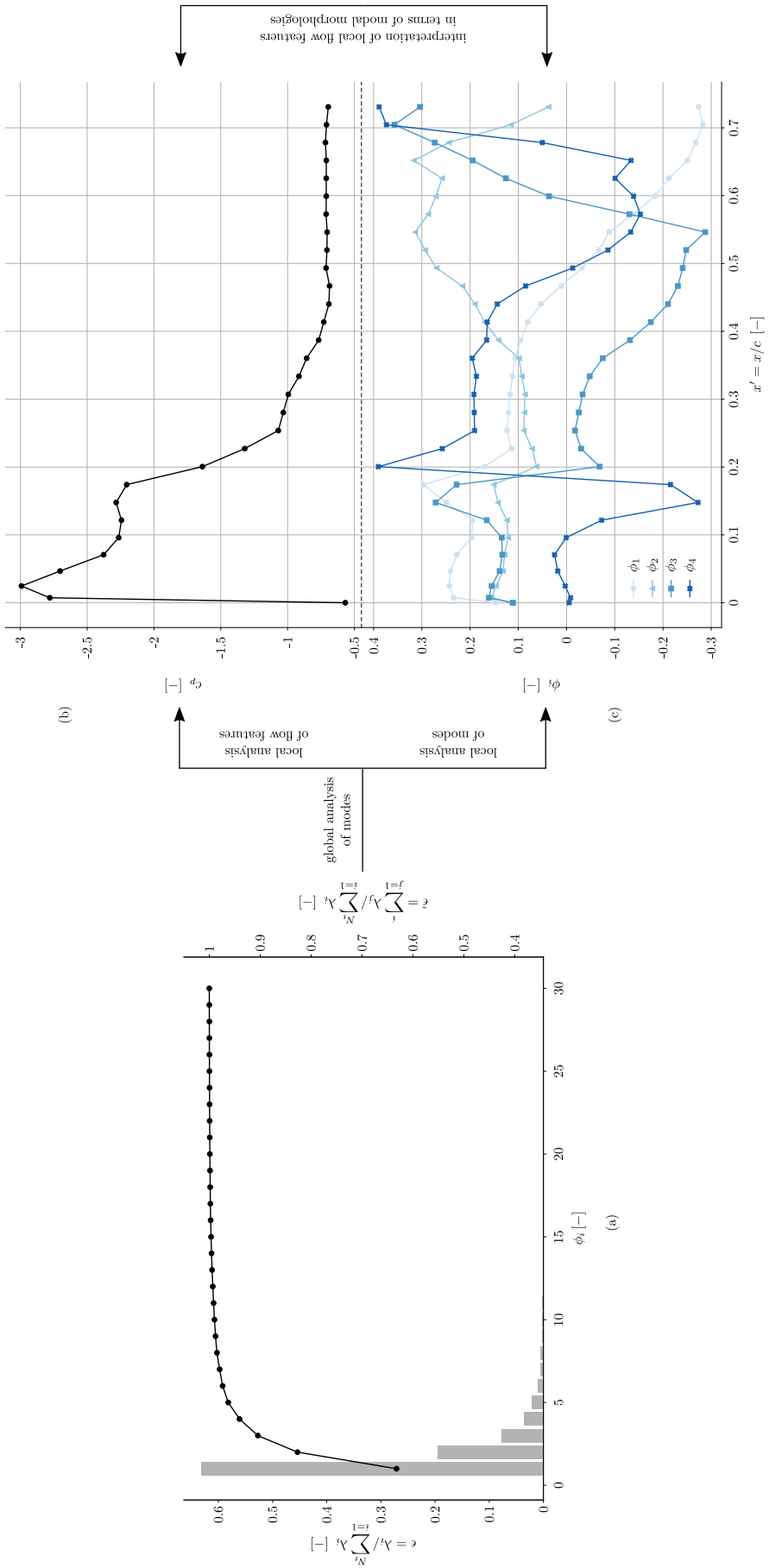

FIG. 4: Layout of a generic modal analysis undertaken for the configuration tested at Re = 1.2×10^5, $\alpha = 12°$; (a) eigenvalues (left $y-$axis) and cumulative eigenvalues (right $y-$axis); (b) chord-wise c_p distribution; (c) chord-wise modal shapes for the first four POD modes.

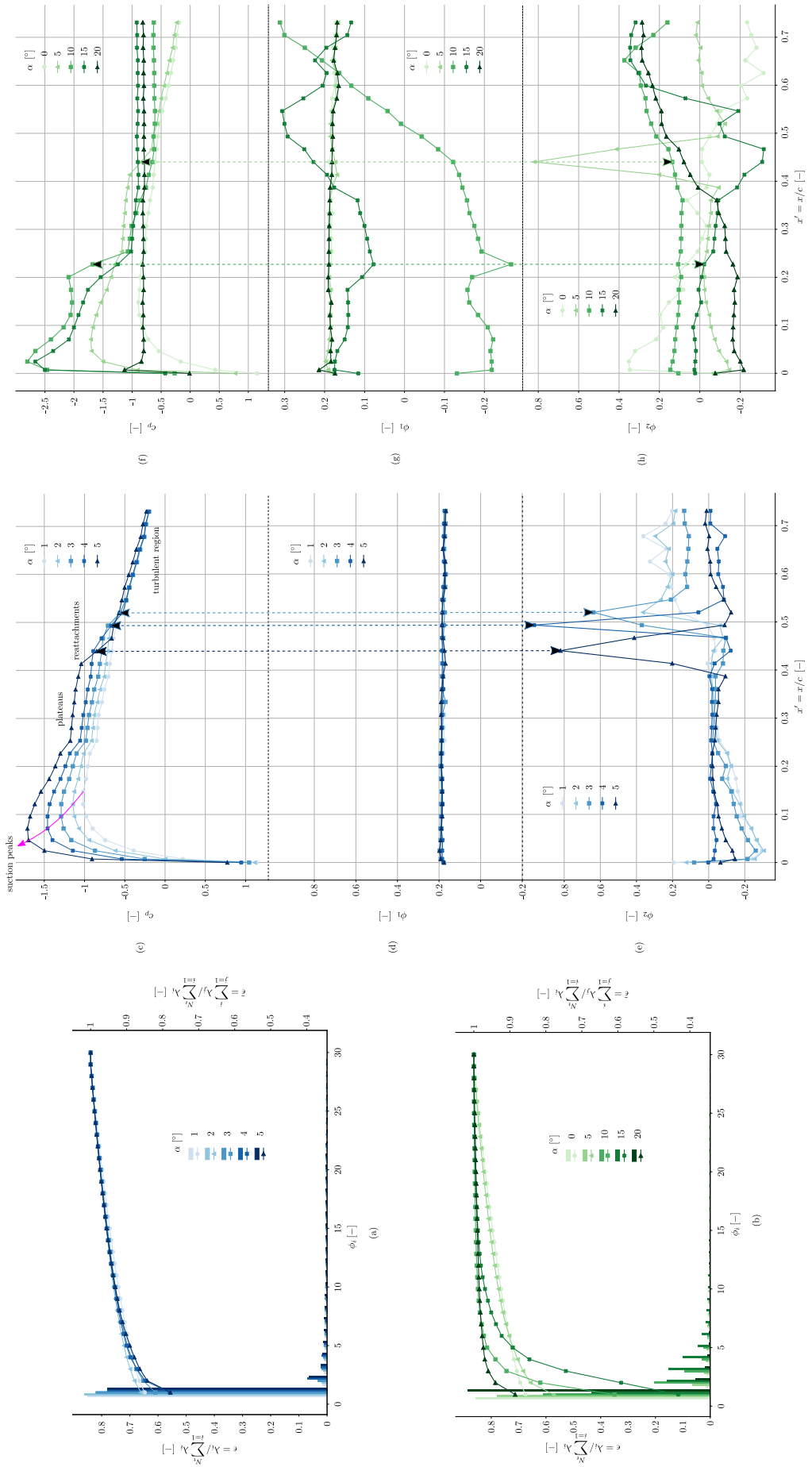

FIG. 5: Sensitivity with respect to α; (a-c-d-e): modal analysis, in the layout set forth in FIG 4, for low angles-of-attack, namely $\alpha \in [1,5]^{\circ}$; (b-f-g-h): modal analysis for the overall range of angles-of-attack, namely $\alpha \in [0,20]^{\circ}$.

with successively higher α values inducing both an ever-larger and an ever-closer suction peak near the leading-edge, a set of gradually smaller plateau-like regions that corresponds to a shrinkage of the LSB structure, and a gradually promoted reattachment phenomenon. More detailed descriptions of the physical mechanisms driving such processes may be found in[40]. With all, the mode that best captures the aerodynamic structures being formed upon the airfoil is the second one, as shown in FIG 5e. In particular, the mode seems to detect the reattachment phenomenon acceptably, whenever such a reattachment occurs with a sufficient re-energizing of the flow as to induce a noticeable pressure recovery in the c_p distributions. For the analyzed cases, the energetic amplitude of the reattachment becomes relevant beyond $\alpha = 3°$, beyond which the modal shape shows an acute peak indicating the occurrence of the LSB closure. In fact, the relevance of the second mode for detecting flow-related features may be translated into the lowering of the first mode's relative value with α, as mentioned when discussing FIG 5a. The steeper initial shapes of the cumulative curves, which are more pronounced for increasing angles-of-attack, are indicative of the larger relevance of the second mode an the ensuing of an energetically stronger reattachment event.

The picture described above changes considerably when analyzing the overall range of angles-of-attack. FIG 5b shows that the modal distributions change considerably when increasing α beyond the aerodynamically linear region. Indeed, when reading such distributions in terms of the c_p curves shown in FIG 5f, it is observed that the closeness to the stalling phenomenon, which occurs for $\alpha = 15°$, induces a gradual decrease on the relative value of the first mode, with the cumulative curve showing a steeper exponential slope confined to the region of the first 5 modes for $\alpha = 10°$. When stalling occurs, such a slope becomes milder and the range of relevant modes is punctually expanded to the first 10 terms. Afterwards, when the airfoil is already operating within the deep post-stall region at $\alpha = 20°$, the first mode recovers its relevance and the cumulative curve flattens acutely. In addition to the mentioned features, it is to notice that the main difference between the low$-$ and high$-\alpha$ regions is the relative weight that high modes achieve. This is particularly remarked by the cumulative curves, which show a nearly constant slope for angles-of-attack lying within the aerodynamically linear region ($\alpha < 8°$). The trend of the curve changes noticeably outside such a region, showing two main tendencies that occur successively: during the post-linear, pre-stall region, the curve is exponential in nature, with a large relevance of the intermediate modes. Within the post-stall region, the exponential shape of the curve is preserved, but the relevance of the modes is constrained to the first few terms. Regardless of the post-linear region being analyzed, though, the flatness of the cumulative curves beyond the 10^{th} mode indicate their negligible contribution to the energetic description of the flow.

In spite of the modal redistribution that occurs in the post-linear, pre-stall region, the analysis carried out in FIGS 5g and 5h is restricted to the first two modes for a couple of reasons. First, because it is observed that the shape of higher modes is not conclusive for describing the flow features shown in the c_p distributions. Second, because constraining the analysis avoids an excessive chartjunk and helps the understanding of the figures. As may be noticed, the lack of sensitivity of the first mode mentioned when dealing with lα values below $7°$ is not applicable anymore. Indeed, such a mode is effective in capturing the reattachment phenomenon for the $\alpha = 10°$ and $15°$ cases. In contrast, such reattachments do not have a counterpart on the second mode, which only serves for determining the LSB closure for the already known $\alpha = 5°$ case.

Besides capturing the reattachment location, the first mode of the $\alpha = 10°$ case shows a steep slope downstream the mid-chord stage. Such a slope is not reproduced equally by the $\alpha = 15°$, mainly due to the fact that it is undergoing stall, but it nevertheless shows a highly fluctuating nature beyond the reattachment point. Likewise, such slopes and fluctuations are reproduced, albeit in a more milder way, in the shapes of the second modes. To the contrary, the $\alpha = 20°$ case shows a flat first mode, although it does manifest a substantial slope beyond mid-chord in the second mode. These observations lead to the conclusion that there are three main regions in the analyzed angular range within which the modal interpretations change: the aerodynamically linear region that corresponds to low α values shows constant first mode shapes, and its second mode serves for capturing the reattachment phenomenon. During the post-linear, pre-stall zone, the first modal shape becomes relevant for detecting reattachment and showing the evolution of the post-reattached turbulent flow, whereas the second mode merely reflects such a turbulent flow in an attenuated manner. Within the post-stall region, where no reattachment occurs whatsoever, the first mode turns constant again, and the second mode regains its descriptive feature, albeit for showing the evolution of the turbulent boundary-layer being developed upon the airfoil.

When confronted with the shapes of the cumulative curves discussed before, the notions laid above for the high α cases may sound counter-intuitive. Indeed, the noticeable loss of the relative importance of the first mode, which ensues when increasing the angle-of-attack beyond the aerodynamically linear region, may lead to thinking that such a mode will not play a role on determining the features of the flow insofar it corresponds, comparatively, to a lower energy-carrying structure. However, the POD analysis performed so far seems to suggest otherwise. Thus, it may be deduced that it is not the most energetic mode the one carrying the fundamental flow-related information. Instead, such a mode must be specified on a configuration-wise basis. No physical mechanism has been found so far for explaining this behavior, but there are two main reasons that can be alleged: first, the undertaken POD analysis is one-dimensional, meaning that the effect of two-dimensional flow features that inherently affect the development of energetic structures are not being accounted for. Second, the strongest modes may be a surrogate for the external flow's average energy, which does not necessarily match the modal structures developed by the LSB. These may be better reflected by higher energy modes during the aerodynamically linear region. Beyond linearity, however, the LSB structure becomes exceedingly short, with its corresponding effect being taken over by the most energetic mode that devel-

ops downstream the reattachment point.

C. Sensitivity to the Reynolds number, Re

The so called scale-effect, or the influence of the Reynolds number of the aerodynamic behavior, is discussed according to the data provided in FIG 6. As mentioned in a previous work by the authors[40], increasing the Reynolds number for the transitionally-operating NACA0021 airfoil promotes an earlier transition and, hence, a shortening of the LSB. This has also been observed at relatively low angles-of-attack, as discussed in FIG 5e, where the upstream displacement of the second POD mode maxima indicates the forward motion of the LSB closure.

However, such an analysis is not as straightforward at angles-of-attack that lie close to or beyond stalling, with the reading of the POD modes becoming less evident. In fact, stalling is observed to alter the spatial distribution of the eigenmodes in a less coherent manner, as reflected in FIG 6. The figure synthesizes the modal analysis for the airfoil operating at an angular configuration of $\alpha = 14^\circ$ and three different Reynolds numbers. The choice of such an angle-of-attack is justified insofar it allows observing the three possible flow conditions that ensue on the suction-side, namely: pre-stall ($\mathrm{Re} = 1.6 \times 10^5$), attached flow($\mathrm{Re} = 1.2 \times 10^5$) and post-stall ($\mathrm{Re} = 8 \times 10^4$).

The analysis of the cumulative curves, plotted in FIG 6a, reveals that an increase of the Reynolds number induces variations on the energy distributions among the POD modes. While at low Reynolds numbers there exists a significant contribution of higher order nodes, requiring close to 10 eigenmodes to recover 90% of the total energy, the opposite is observed when Reynolds is increased. The first modes gain energy in detriment of the subsequent ones, with 3 eigenmodes recovering the same total energy on a flow configuration near stall conditions at $\mathrm{Re} = 1.6 \times 10^5$. This is reflected in the shape of the curves, with the 80k case showing a wider constant-slope region than the 1.2×10^5 and 160k cases, which show a much more exponential trend that confines the modal contributions to the first few modes, with a flat morphology developing afterwards.

The Reynolds-dependent LSB behavior can be analyzed in modal terms with the aim of FIGS 6c and 6d, which depict the third and fifth POD modes respectively. If read together with the c_p distributions shown in FIG 6b, the eigenmode shapes reveal a non-intuitive energy distribution of the physically related modes. It was discussed in Section IV B that, up to values of $\alpha \approx 10^\circ$, the LSB-related eigenmode gained relative energy with increasing angles-of-attack. However, the behavior near the stall condition suggests otherwise. Both the larger pressure fluctuations near stall and the homogenization effect due to an increase in Reynolds number, displace the characteristic peak associated to the LSB closure to higher modal contributions, spreading it altogether across several modes. When interpreting this fact together with the previously mentioned energy distribution of the POD modes occurring for higher Reynolds numbers, the relative energy of the eigenmodes associated with the LSB closure are shown to drop. At $\mathrm{Re} = 1.2 \times 10^5$, the peak indicating flow reattachment appears for both the third and the fifth mode, while at $\mathrm{Re} = 1.6 \times 10^5$ it manifests appreciably in the fifth mode, whereas the drop in the third mode, although discernible, becomes milder.

Besides the modal description provided above, it is to notice that the shapes of the eigenmodes show considerable variations in magnitude beyond the mid-chord stage, suggesting large pressure fluctuations near the trailing-edge of the airfoil. This fact agrees with the development of the turbulent boundary-layer beyond the reattachment point, and the oscillation of the modal shapes are indicative of the inherently fluctuating behavior of turbulent structures. However, care must be taken when making a comparative between the magnitudes of both modes. The post-processing stage of the POD decomposition devises a normalization operation whereby the modal values are scaled with the relative energy of their corresponding eigenmodes. Hence, neither the sign nor the amplitude is comparable between the POD modes, just their respective phases. On these grounds, the joint interpretation of the modes is solely qualitative, which, on the other hand, suffices for relating them to the main flow features observed in the c_p distributions, as noted above.

D. Sensitivity to surface roughness

The comparative between clean and rough cases is carried out on the grounds of FIG 7. For the sake of conciseness, the modal analyses of the plots comprise the two sets of flow configurations operating at $\mathrm{Re} = 1.2 \times 10^5$. Besides, the layout of the plots follows the structure of FIG 5, meaning that a subset of the plots refers to low angular configurations (namely FIGS 7a and 7c to 7e), and the other to large angles-of-attack (i.e. FIGS 7b and 7f to 7h).

As observed in a previous work by the authors, the presence of leading-edge roughness promotes an earlier saturation as the Reynolds number increases[36]. Likewise, the same research shows an inversion of the natural tendency of the maximum lift coefficient values, with this parameter becoming smaller as the Reynolds number increased. The hysteresis phenomenon is also shown to be severely modified when roughness is applied, being totally suppressed for the highest values of the Reynolds numbers considered herein.

The translation of such flow features to the c_p distributions discussed in the present work is clearly observed in the distinctive kink related to the roughness effect, as shown in FIG 7c. The presence of such a kink, which has been shown not to be associated with the end of the roughness band anyway, may blur the identification of the LSB in the transitional regime. Surface flow visualizations could not confirm the presence of LSB-like structures and, consequently, the c_p features have been taken as an indicative of a more effective sweeping linked to the reattachment phenomenon[36].

On this respect, a remarkable difference between clean and rough configuration arises when considering the number of modes that need to be recovered in order to assess the occurrence of reattachment. Section IV B asserted that retaining the

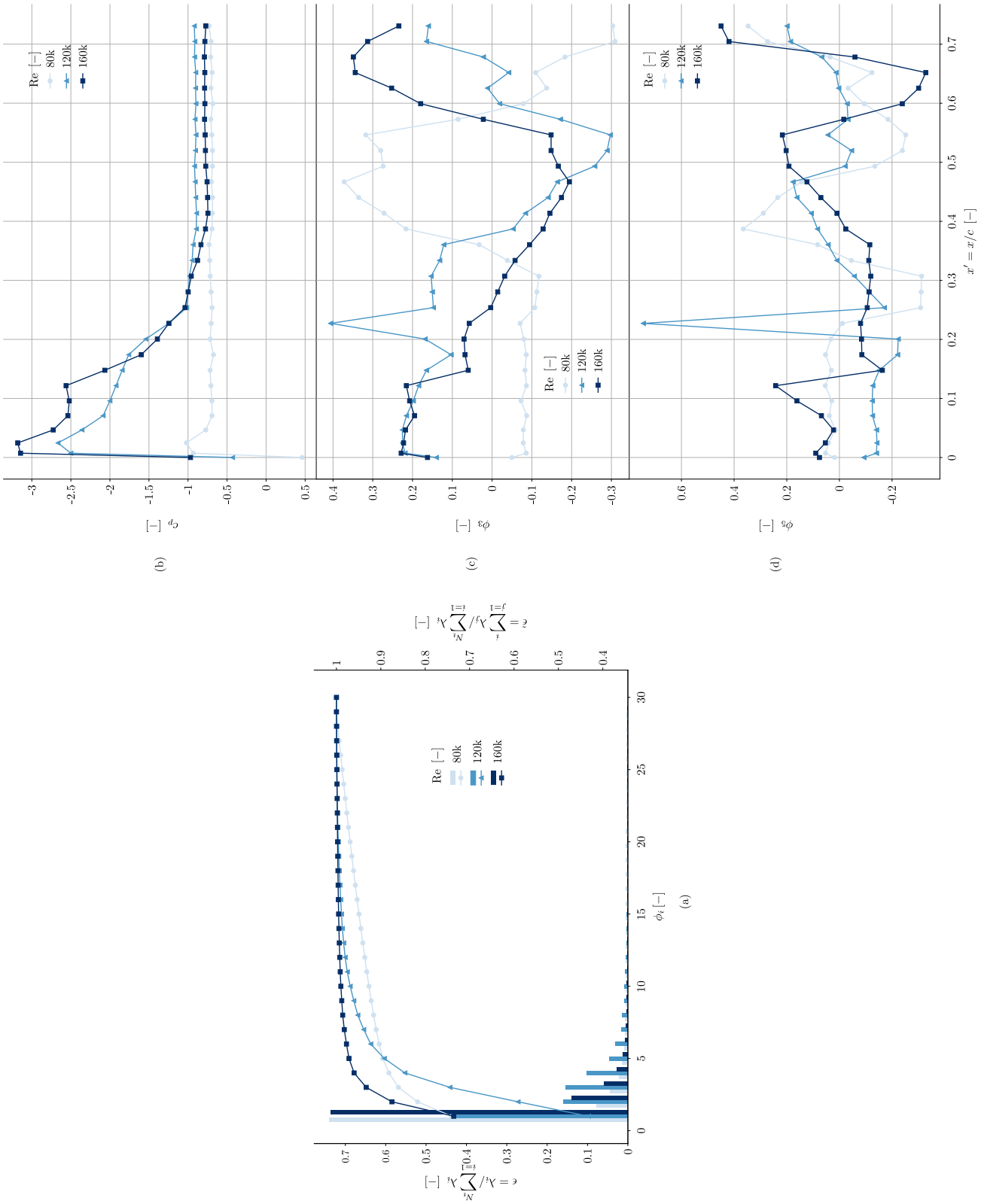

FIG. 6: Sensitivity with respect to Re for a fixed angle-of-attack $\alpha = 14°$, in the layout set forth in FIG 4, for Reynolds numbers $\mathrm{Re} \in [8 \times 10^4, 1.6 \times 10^5]$. Modal analysis shows (c) third eigenmode and (d) fifth eigenmode spatial distributions.

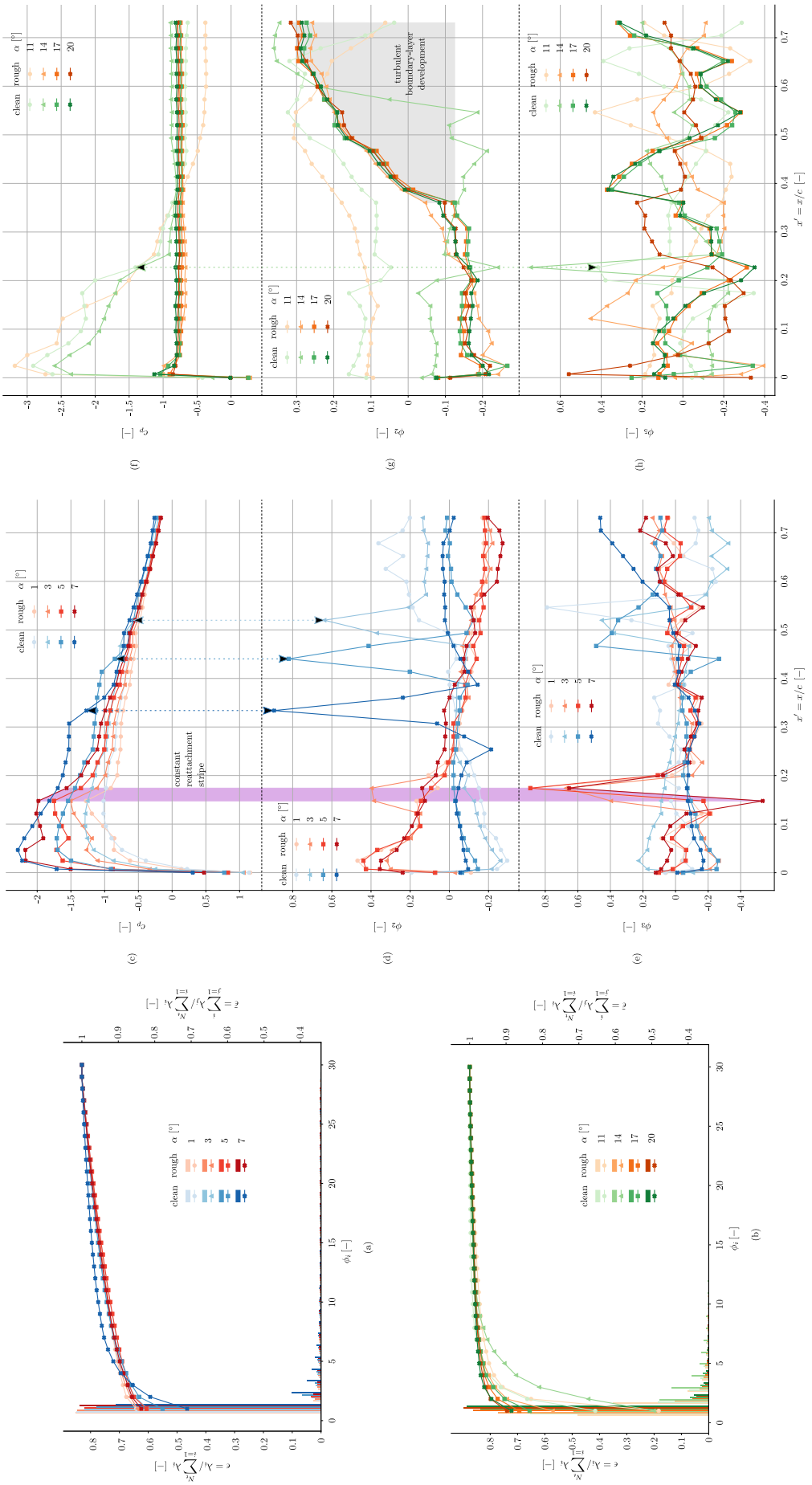

FIG. 7: Comparative analysis of clean and rough configurations at $\mathrm{Re} = 1.2 \times 10^5$; (a-c-d-e): comparative modal analysis, for low angles-of-attack, namely $\alpha \in [1,7]^\circ$; (b-f-g-h): comparative modal analysis for high angles-of-attack, namely $\alpha \in [11,20]^\circ$.

first two modes is sufficient for such a purpose when dealing with clean configurations. To the contrary, FIGS 7d and 7e show that, for rough configurations, extending the analysis to the third mode becomes necessary at low α values. The increase in the mode order associated to the fluctuations produced on the reattachment location becomes more relevant as the angle-of-attack grows. Indeed, FIG 7h shows that it is necessary to represent the fifth mode for capturing features related to reattachment when going beyond $\alpha = 11^\circ$. Besides, it is to notice the role played by the second mode at large angles-of-attack, as shown in FIG 7g. As observed, such a mode does not provide information on the reattachment location except for the pre-stalled clean configurations. In the case of the stalled configurations, the corresponding modal shapes manifest a sustained increase from mid-chord onward. Such a growth, which has already been discussed in Section IV C, is related to the development of the turbulent boundary-layer. However, it is relevant to highlight that, apparently, the turbulent boundary-layer is insensitive to both the angular configuration and the flow paradigm beyond a given angle-of-attack. Additionally, it is to mention that such a lack of sensitivity is also found when varying the Reynolds number, although the corresponding figures have not been included for two main reasons: first, because the conclusions drawn from the observed features match the ones discussed in Section IV C. And second, for avoiding enlarging the research exceedingly.

Finally, a relevant characteristic of the analysis has to do with a flow feature that was also identified on the experimental campaign carried out by the authors[36], namely the invariability of the reattachment location with the angle-of-attack. This tendency is reproduced in the POD decomposition, as depicted in FIG 7c. The physical origin of this phenomenon still remains unclear, as there is no sufficient data to elucidate if the separation- and-reattachment invariability is produced by an earlier transition induced by the surface roughness, or due to the geometrical effects of the roughness band placed at the leading-edge. What becomes clear from both the experimental data and the numerical analysis performed herein, is that the presence of the roughened region induces a mixing and homogenization of the pressure fluctuations downstream the band, which is reflected on the energetic spreading across the POD modes.

E. Reduced-order model analysis

In this section, a reduced-order model (ROM) approach is employed to evaluate the number of eigenvectors required to properly recover the flow physics related with the reattachment phenomenon. This procedure can also be used to analyze or verify which eigenvector would have the greatest influence on the ROM accuracy. The reduced-order model study complements the modal analysis carried out in the previous sections since, as expression (Equation (8)) shows, it not only considers the modes but also their temporal data-series and, therefore, the energy of each one. Thus, this ROM analysis considers both the eigenvectors and their associated energy together.

The cases considered correspond to two angles-of-attack, namely $\alpha = 4^\circ$ and 10°, for each of the clean and rough configurations operating at a Reynolds number of 1.2×10^5. Hence, four data-series are analyzed. For each data-series, ROMs with different orders have been generated, starting with a ROM that pertains to the first mode alone (order 1), and successively adding the information contained in further eigenmodes in a cumulative manner and complying with the POD-specific ordering of ever-decreasing relative energy. For illustrative purposes, the original experimental data (non-reduced, as it contains all the physical information), is denoted as the complete model (CM).

To analyze the influence of each mode on the reattachment phenomenon, the corresponding temporal data-series of the pressure tap closest to the reattachment point are employed in the ROM generation. For the clean configurations at $\alpha = 4^\circ$ and 10°, such a tap is located at a dimensionless distance of $x' \approx 0.45$ and $x' \approx 0.20$, respectively. In the case of the rough configurations, the corresponding position becomes fixed at $x' \approx 0.17$, as mentioned in Section IV D. As the ROM order increases, the resulting recovered data-series would approach the complete model. To quantify the similarity between the ROM and the complete model, a relative error is defined by means of the standard deviation of the data-series, σ, as:

$$\varepsilon = \frac{|\sigma_{ROM} - \sigma_{CM}|}{\sigma_{CM}} \tag{9}$$

FIG 8 represents such an error parameter as a function of the ROMs order for the analyzed configurations. It is observed that the clean configuration operating at $\alpha = 4^\circ$ shows a significant ε reduction when including the second POD mode. This shows that such a mode carries the information related to the reattachment phenomenon. To the contrary, the rough configuration running at the same angle-of-attack requires three modes for properly recovering the fluctuations induced by the LSB closure. This implies that, for the rough case, the eigenvector associated with the reattachment phenomenon carries less energy. This outcome agrees with results discussed in Section IV D, where reattachment has been detected by the second eigenvector for the clean cases, whereas skipping to the third eigenvector has been necessary for the rough cases at low angles-of-attack.

Increasing α values require including higher order eigenvectors in the ROMs to recover the pressure fluctuations caused by the reattachment phenomenon. Therefore, for a configuration with $\alpha = 10^\circ$, fifth or even eighth order ROMs are required for the clean and rough flow configurations, respectively. Thus, the relative energy of eigenvectors related to the LSB closure decrease with the angle-of-attack. Moreover, this decrease in energy is followed by a gradual reduction in relative error as the ROMs order increases, so that the reattachment phenomenon is spread over a larger number of eigenvectors. Thus, for clean case at $\alpha = 4^\circ$ only the second mode is needed to correctly recover the data-series and this mode reduces the relative error by more than 40%, while for $\alpha = 10^\circ$ the third, fourth and fifth modes are needed to recover the signal and each eigenvector influences the relative error by about 10%. The spread of the reattachment phenomenon in

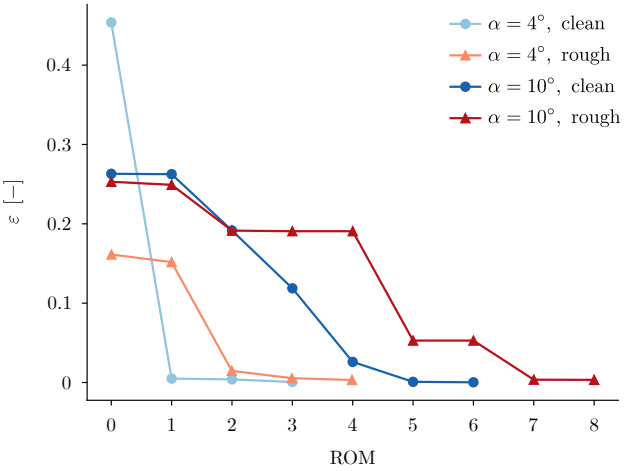

FIG. 8: Relative error of the standard deviation, ε, as a function of the ROMs order for different angle-of-attack and surface configurations, without (C) or with (R) roughness.

different eigenvectors for large angles-of-attack has also been identified in previous sections through modal shapes analysis. Thus, in figure FIG 6 it was already suggested that the LSB closure participated in both the third and fifth eigenvectors due to the amplitude maxima they present in $x' \approx 0.22$. Therefore, this tendency is confirmed when analysing the reduced-order models.

From the analysis of the low-order models, it can be concluded that rough configurations require a larger number of modes to correctly recover the reattachment phenomenon. Therefore, the presence of roughness or an increase of the angle-of-attack reduces the relative energy of the eigenvectors related to this phenomenon.

V. CONCLUSIONS AND FUTURE WORKS

The influence of the Reynolds number, angle-of-attack and surface roughness on the spatial distribution and relative energy of POD modes calculated through a modal decomposition of experimental pressure coefficient time series measured over a symmetrical airfoil has been analyzed. Within the framework of an experimental campaign aimed to investigate laminar to turbulent transition phenomena, direct observation and forces monitoring[19] is complemented here with a data-driven post processing of surface pressure data. Additionally, reduced-order-models (ROM) are generated and the influence of higher order modes on their accuracy is evaluated. The main findings of the research are listed below:

- The POD analysis upon a collection of experimentally obtained data-sets reveals spatial structures that can be related to the presence of a LSB on the suction side of the tested NACA 0021 airfoil.
- While the first four POD modes store about 90% of the signal energy, suggesting to delimit the modal analysis to a few orthogonal components in most cases, it has been found that the fluctuations related to the LSB may appear in high order modes and compromise the ROM accuracy.
- The reattachment or closure of the LSB correlates with high pressure deviations that are captured by the eigenmodes, with its upstream motion with increasing angles-of-attack or Reynolds number being reflected on distributions of the modes. In particular, the second mode is a well-suited indicator for determining the LSB in clean surface configurations without detached flows.
- Increasing the Reynolds number provokes an heterogeneous relative energy distribution of the eigenmodes, with the low order modes gaining energy in detriment of the subsequent ones.
- To the contrary, the presence of leading-edge roughness induces a spread-out effect of the eigenvalues, displacing the mode physically related to the LSB closure to modes with lower relative energy.
- ROMs constitute a proper technique for recovering the information stored in the temporal data-series for reproducing the most energetic structures of the flow configuration.

Nevertheless, the insights provided by the analysis open possible research lines that are to be undertaken in a near future. In particular:

- The shape of the first POD mode is constant at low angles of attack, indicating homogeneous fluctuations along the upper surface. Providing a physical interpretation of this mode requires further tests for determining the turbulent length scale of the configurations. Additionally, it is deemed necessary to measure the pressure distributions at the suction and pressure sides of the airfoil simultaneously.
- The modal analysis can be extended to global variables such as the lift and drag coefficients of the airfoil. Such measurements may provide further insights as for the evolution of the modes and their underlying physical interpretation.
- Performing CFD simulations upon the virtual twin of the experimental configuration can turn useful as far as a proper numerical-experimental matching is obtained on the analyzed cases. If so, further configurations may rely exclusively on a CFD analysis, dispensing additional experimental testing campaigns.

VI. DATA AVAILABILITY STATEMENT

The data that support the findings of this study are available from the corresponding author upon reasonable request.

VII. ACKNOWLEDGEMENTS

The authors gratefully acknowledge the financial support from the Department of Education of the Basque Government for the Research Grant [PRE_2017_1_0178] and the Research Group [No. IT1505-22], and the Economic Development, Sustainability and Environment Department of the Basque Government under the Grant No. KK-2022/00105 (ELKARTEK).

[1] T. Mueller and J. DeLaurier, "Aerodynamics of small vehicles," Annual Review of Fluid Mechanics **35** (2003).

[2] R. J. Volino and C. G. Murawski, "Separated flow transition in a low pressure turbine cascade - Mean flow and turbulence spectra," American Society of Mechanical Engineers, International Gas Turbine Institute, Turbo Expo (Publication) IGTI **5 B**, 821–832 (2003).

[3] S. Watkins, S. Ravi, and B. Loxton, "The effect of turbulence on the aerodynamics of low Reynolds number wings," Engineering Letters **18** (2010).

[4] L. Petricca, P. Ohlckers, and C. Grinde, "Micro- and nano-air vehicles: State of the art," International Journal of Aerospace Engineering **2011**, 1–17 (2011).

[5] K. W. Van Treuren, "Small-Scale Wind Turbine Testing in Wind Tunnels Under Low Reynolds Number Conditions," Journal of Energy Resources Technology **137** (2015).

[6] D. L. Shukla, A. U. Mehta, and K. V. Modi, "Dynamic overset 2d cfd numerical simulation of a small vertical axis wind turbine," International Journal of Ambient Energy **41**, 1415–1422 (2020).

[7] J. Sun, X. Sun, and D. Huang, "Aerodynamics of vertical-axis wind turbine with boundary layer suction – effects of suction momentum," Energy **209**, 118446 (2020).

[8] X. Zhang, Z. Li, X. Yu, and W. Li, "Aerodynamic Performance of Trailing-Edge Modification of H-Type VAWT Blade Considering Camber Effect," International Journal of Aeronautical and Space Sciences **21**, 587–598 (2020).

[9] F. Balduzzi, D. Holst, P. F. Melani, F. Wegner, C. N. Nayeri, G. Ferrara, C. O. Paschereit, and A. Bianchini, "Combined numerical and experimental study on the use of gurney flaps for the performance enhancement of naca0021 airfoil in static and dynamic conditions," Journal of Engineering for Gas Turbines and Power **143** (2021).

[10] J. Sun and D. Huang, "Numerical investigation of boundary layer suction control positions on airfoils for vertical-axis wind turbine," Journal of Mechanical Science and Technology **35**, 2903–2914 (2021).

[11] J. Winslow, H. Otsuka, B. Govindarajan, and I. Chopra, "Basic understanding of airfoil characteristics at low Reynolds numbers (104–105)," Journal of Aircraft **55**, 1050–1061 (2018).

[12] G. Ananda, *Aerodynamic performance of low-to-moderate aspect ratio wings at low Reynolds numbers*, Ph.D. thesis, University of Illinois at Urbana-Champaign (2012).

[13] K. L. Hansen, R. M. Kelso, A. Choudhry, and M. Arjomandi, "Laminar Separation Bubble Effect on the Lift Curve Slope of an Airfoil," in 19^{th} *Australasian Fluid Mechanics Conference* (Melbourne, 2014) pp. 1–4.

[14] A. Choudhry, M. Arjomandi, and R. Kelso, "A study of long separation bubble on thick airfoils and its consequent effects," International Journal of Heat and Fluid Flow **52** (2015).

[15] M. C. Galbraith and M. R. Visbal, "Implicit large eddy simulation of low Reynolds number flow past the SD7003 airfoil," 46th AIAA Aerospace Sciences Meeting and Exhibit , 1–17 (2008).

[16] G. Corten and H. Veldkamp, "Insects Cause Double Stall," European Wind Energy Conference 2001 , 470–474 (2001).

[17] M. G. Khalfallah and A. M. Koliub, "Effect of dust on the performance of wind turbines," Desalination **209**, 209–220 (2007).

[18] M. Kok, T. Mertens, D. Raps, and T. M. Young, "Influence of surface characteristics on insect residue adhesion to aircraft leading edge surfaces," Progress in Organic Coatings **76**, 1567–1575 (2013).

[19] A. Zarketa-Astigarraga, M. Penalba, A. Martin-mayor, and M. Martinez-agirre, "Experimental assessment of scale-effects on the aerodynamic characterization of a transitionally-operating airfoil working under clean flow conditions," Measurement **188**, 110414 (2022).

[20] A. Zarketa-Astigarraga, M. Penalba, A. Martin-Mayor, and M. Martinez-Agirre, "Impact of turbulence and blade surface degradation on the annual energy production of small-scale wind turbines," (2022).

[21] A. Koodly Ravishankara, H. Özdemir, and E. van der Weide, "Analysis of leading edge erosion effects on turbulent flow over airfoils," Renewable Energy **172**, 765–779 (2021).

[22] P. Saathoff and W. Melbourne, "Freestream turbulence and wind tunnel blockage effects on stream wise surface pressures," Journal of Wind Engineering and Industrial Aerodynamics **26**, 527–544 (1987).

[23] J. A. Cardenas-Rondón, M. Ogueta-Gutierrez, S. Franchini, and O. Gomez-Ortega, "Experimental analysis of the aerodynamic characteristics of a rectangular 5: 1 cylinder using pod," Wind and Structures **34**, 29–42 (2022).

[24] G. De Cillis, S. Cherubini, O. Semeraro, S. Leonardi, and P. De Palma, "Stability and optimal forcing analysis of a wind turbine wake: Comparison with POD," Renewable Energy **181**, 765–785 (2022).

[25] "A three-dimensional dynamic mode decomposition analysis of wind farm flow aerodynamics," Renewable Energy **191**, 608–624 (2022).

[26] P. Liu, G. Yu, X. Zhu, and Z. Du, "Unsteady aerodynamic prediction for dynamic stall of wind turbine airfoils with the reduced order modeling," Renewable Energy **69**, 402–409 (2014).

[27] Q. Wang, Z. X. Wang, J. J. Song, Y. Xu, and J. Z. Xu, "Study on a new aerodynamic model of HAWT based on panel method and Reduced Order Model using Proper Orthogonal Decomposition," Renewable Energy **48**, 436–447 (2012).

[28] M. Gaster, "The Structure and Behaviour of Laminar Separation Bubbles," Tech. Rep. (Aeronautical Research Committee (ARc), London, UK, 1967).

[29] M. Zhao, Y. Zhao, Z. Liu, and J. Du, "Proper Orthogonal Decomposition Analysis of Flow Characteristics of an Airfoil with Leading Edge Protuberances," AIAA Journal **57**, 2710–2721 (2019).

[30] L. Shi, H. Ma, and X. Yu, "POD analysis of the unsteady behavior of blade wake under the influence of laminar separation vortex shedding in a compressor cascade," Aerospace Science and Technology **105**, 106056 (2020).

[31] G. Huang, Y. Dai, and C. Yang, "Energy extraction in the dynamic modes of flow for airfoil's laminar separation flutter," Physics of Fluids **34**, 083601 (2022).

[32] M. Zhao, Y. Zhao, and Z. Liu, "Dynamic mode decomposition analysis of flow characteristics of an airfoil with leading edge protuberances," Aerospace Science and Technology **98**, 105684 (2020).

[33] Y. Zhang, J. Xu, Y. Li, L. Qiao, and J. Bai, "Modeling of surface roughness effects on bypass and laminar separation bubble-induced transition for turbomachinery flows," Physics of Fluids **34**, 044108 (2022).

[34] I. Torrano, *Low speed wind tunnel design, setup, validation and testing of airfoils in turbulent in ow conditions*, Ph.D. thesis, Mondragon Goi Eskola Politeknikoa (2016).

[35] A. Zarketa-Astigarraga, A. Martin-Mayor, and M. Martinez-Agirre, "Experimental uncertainty decompositions of aerodynamic coefficients affected by operative condition variations," Measurement **165**, 1–14 (2020).

[36] A. Zarketa-Astigarraga, *Aerodynamic Characterization of Transitionally-Operating Airfoils under a set of Flow Conditions going from Ideal to Real Configurations*, Ph.D. thesis, Mondragon Unibertsitatea (2021).

[37] A. Vaidyanathan, D. Kingman, and T. Kurth, "When do endplates work?" in 52^{nd} *Aerospace Sciences Meeting* (2014) pp. 1–11.

[38] J. B. Barlow, W. H. Rae, and A. Pope, *Low-speed wind tunnel testing*, 3rd ed. (John Wiley & Sons, Inc., 1999) p. 724.

[39] C. Tropea, A. L. Yarin, and J. F. Foss, "Pressure Measurement Systems," in *Springer Handbook of Experimental Fluid Mechanics* (Springer, Berlin, 2007) 1st ed., Chap. 4, pp. 179–214.

[40] A. Zarketa-Astigarraga, A. Martin-Mayor, M. Martinez-Agirre, and M. Peñalba-Retes, "Assessing the statistical validity of momentum-deficit-based c_D measurements in turbulent configurations," Measurement **181** (2021).

[41] A. Zarketa-Astigarraga, A. Martin-Mayor, and M. Martinez-Agirre, "Theoretical concepts for describing a replication-levels-based uncertainty analysis approach," in *Advances in Measurements and Instrumentation: Reviews, Book Series, Vol. 2*, edited by S. Yurish (IFSA Publishing, 2020) 1st ed.

[42] J. D. Holmes, "Analysis and synthesis of pressure fluctuations on bluff bodies using eigenvectors," Journal of Wind Engineering and Industrial Aerodynamics **33**, 219–230 (1990).

[43]G. Berkooz, P. Holmes, and J. L. Lumley, "The proper orthogonal decomposition in the analysis of turbulent flows," Annual Review of Fluid Mechanics **25**, 539–575 (1993).

[44]Y. C. Liang, H. P. Lee, S. P. Lim, W. Z. Lin, K. H. Lee, and C. G. Wu, "Proper Orthogonal Decomposition and Its Applications—Part I: Theory," Journal of Sound and Vibration **252**, 527–544 (2002).

[45]B. W. van Oudheusden, F. Scarano, N. P. van Hinsberg, and D. W. Watt, "Phase-resolved characterization of vortex shedding in the near wake of a square-section cylinder at incidence," Experiments in Fluids. **39**, 86–98 (2005).

[46]A. Kareem, C. Cheng, and P. Lu, "Pressure and force fluctuations on isolated circular cylinder of finite height in boundary layer flows," J. Fluids Struct **3**, 481–508 (1989).

[47]A. Kareem and C. M. Cheng, "Pressure and Force Fluctuations on Isolated Roughened Circular Cylinders of Finite Height in Boundary Layer Flows," J. Fluids Struct **13**, 907–933 (1999).

[48]S. Le Clainche, D. Rodríguez, V. Theofilis, and J. Soria, "Flow around a hemisphere-cylinder at high angle of attack and low reynolds number. part ii: Pod and dmd applied to reduced domains," Aerospace Science and Technology **44**, 88–100 (2015), instability and Control of Massively Separated Flows.

[49]O. T. Schmidt and T. Colonius, "Guide to spectral proper orthogonal decomposition," AIAA Journal **58**, 1023–1033 (2020).

[50]H. R. Karbasian, J. A. Esfahani, A. M. Aliyu, and K. C. Kim, "Numerical analysis of wind turbines blade in deep dynamic stall," Renewable Energy **197**, 1094–1105 (2022).

[51]H. Tong and Y. Wang, "Experimental study on unsteady aerodynamic characteristics of deformed blades for vertical axis wind turbine," Renewable Energy **173**, 808–826 (2021).

[52]M. Zhang, Q. Wu, G. Wang, B. Huang, X. Fu, and J. Chen, "The flow regime and hydrodynamic performance for a pitching hydrofoil," Renewable Energy **150**, 412–427 (2020).

[53]J. Meseguer-Ruiz and Á. Sanz-Andrés, "Procedimientos para determinar numéricamente la resistencia," in *Aerodinámica Básica* (Garceta Grupo Editorial, 2012) 2nd ed., Chap. 9.2, pp. 262–264.

[54]M. Thompson, *The Small Scales of Turbulence in Atmospheric Winds At Heights Relevant To MAVS*, Ph.D. thesis, RMIT University (2012).

[55]J. Schottler, N. Reinke, A. Hölling, J. Whale, J. Peinke, and M. Hölling, "On the impact of non-Gaussian wind statistics on wind turbines — an experimental approach," Wind Energy Science Discussions , 1–21 (2016).

[56]A. KC, J. Whale, and T. Urmee, "Urban wind conditions and small wind turbines in the built environment: A review," Renewable Energy **131**, 268–283 (2019).

[57]"Labview software main page," ().

[58]"National instruments main page," ().

[59]Y. Zhu, Y. Ju, and C. Zhang, "Proper orthogonal decomposition assisted inverse design optimisation method for the compressor cascade airfoil," Aerospace Science and Technology **105**, 105955 (2020).